energies

MDPI

Article

Study on the Impacts of Capillary Number and Initial Water Saturation on the Residual Gas Distribution by NMR

Tao Li [1], Ying Wang [1,2,*], Min Li [1,*], Jiahao Ji [1], Lin Chang [1,2] and Zheming Wang [2]

[1] State Key Laboratory of Oil and Gas Reservoir Geology and Exploitation, Southwest Petroleum University, Chengdu 610500, China

[2] Pacific Northwest National Laboratory, 902 Battelle Boulevard, P.O. Box 999, MSIN K8-96, Richland, WA 99352, USA

* Correspondence: ywang@swpu.edu.cn (Y.W.); hytlxf@swpu.edu.cn (M.L.); Tel.: +86-028-83034269 (Y.W. & M.L.)

Received: 14 May 2019; Accepted: 12 July 2019; Published: 16 July 2019

Abstract: The determination of microscopic residual gas distribution is beneficial for exploiting reservoirs to their maximum potential. In this work, both forced and spontaneous imbibition (waterflooding) experiments were performed on a high-pressure displacement experimental setup, which was integrated with nuclear magnetic resonance (NMR) to reveal the impacts of capillary number (*Ca*) and initial water saturation (S_{wi}) on the residual gas distribution over four magnitudes of injection rates (Q = 0.001, 0.01, 0.1 and 1 mL/min), expressed as *Ca* (log*Ca* = −8.68, −7.68, −6.68 and −5.68), and three different S_{wi} (S_{wi} = 0%, 39.34% and 62.98%). The NMR amplitude is dependent on pore volumes while the NMR transverse relaxation time (T_2) spectrum reflects the characteristics of pore size distribution, which is determined based on a mercury injection (MI) experiment. Using this method, the residual gas distribution was quantified by comparing the T_2 spectrum of the sample measured after imbibition with the sample fully saturated by brine before imbibition. The results showed that capillary trapping efficiency increased with increasing S_{wi}, and above 90% of residual gas existed in pores larger than 1 μm in the spontaneous imbibition experiments. The residual gas was trapped in pores by different capillary trapping mechanisms under different *Ca*, leading to the difference of residual gas distribution. The flow channels were mainly composed of micropores (pore radius, r < 1 μm) and mesopores (r = 1–10 μm) at log*Ca* = −8.68 and −7.68, while of mesopores and macropores (r > 10 μm) at log*Ca* = −5.68. At both S_{wi}= 0% and 39.34%, residual gas distribution in macropores significantly decreased while that in micropores slightly increased with log*Ca* increasing to −6.68 and −5.68, respectively.

Keywords: capillary number; initial water saturation; capillary trapping; residual gas distribution; nuclear magnetic resonance

1. Introduction

Gas reservoir with aquifers is one of the most common type of reservoirs, in which edge-bottom water entering and fingering often occur, leading to residual gas becoming trapped [1]. A major difficulty in studying gas-water flow in reservoirs is the emergence of trapped phases [2]. Faced with increasing global energy demand, further understanding of gas-water migration characteristics in gas reservoirs is not only beneficial for ensuring the trapping mechanism, but also for optimizing production parameters to exploit reservoirs to their maximum potential [3,4].

Because of the strong compressibility and good fluidity (related to the smaller viscosity of gas) of gas, the experiment for gas-water flow usually encounters more difficulties than liquid flow [5]. Many

experimental studies have been carried out on imbibition (waterflooding) in reservoir samples, including both spontaneous imbibition [6,7] and forced imbibition [8,9]. The relationship between the amount of water into samples and the time it takes are first concerned in the imbibition experiments [10], while the water content is usually evaluated by the weighing method. The gas-phase saturation remaining in porous media is referred to as residual gas saturation (S_{gr}) as the gas phase relative permeability reduces to zero [3]. Numerous relationships between S_{gr} and other petrophysical properties, such as porosity [6,11], permeability [7], clay mineral components [6], pore types [12], heterogeneity [13], S_{wi} (namely water-phase saturation in porous media at the beginning of experiment) [12], etc., have been established. Among them, the S_{wi} of reservoirs refers to the percentage of water volume in reservoir rock to their total pore volume before exploitation, which is an important parameter to evaluate the geological reserves and flow capacity of reservoirs. However, some of the above correlations were found to behave consistently under various rock conditions, few are universally applicable. Also, the residual gas distribution in sample cannot be obtained via the weighing method.

Subsequently, the gas-water imbibition was conducted in micromodels [1]. The process of water-gas migration and the residual gas distribution in micromodels were observed visually via μ-CT [5,14], X-ray [10,15,16] or microscope technique experiments [8]. During the process of imbibition, the variation of water-gas interface geometry in porous media are extremely complicated [1], and some of the gas is immobile due to capillary forces [5,17]. The capillary trapping strongly depends on the core-scale capillary number (expressed as Ca, characterizing the ratio of viscous forces to capillary forces, $Ca = \frac{\mu_w v_w}{\phi \sigma_{gw}}$) [18–21], where μ is water viscosity (Pa·s); v_w is the flow velocity of water, (m/s); ϕ is rock porosity; σ_{gw} represents the interface tension of gas and water (N/m). At different development stages of gas reservoirs, Ca and water saturation are changing. Meanwhile, the capillary forces and gas production in water-bearing samples are related to the water content [22]. Based on micro-CT technology, Mohammadian et al. [23] studied the magnitude and structure of the residual gas phase at the pore scale. With X-ray microtomography, Buchgraber et al. [24] studied the saturation of trapped CO_2 in 2D micromodels for Ca from 10^{-8} to 10^{-5} and found it decreasing continuously as Ca increased, Geistlinger et al. [2] quantified the gas-water interface and the different shapes of isolated gas clusters. Also, with 2D micromodels, Geistlinger et al. [18,25] illustrated that the linear surface-volume relationship of trapped gas clusters, and found that the morphology and number of trapped gas clusters change with Ca. In addition, Herring et al. [26] found that there was a linear relationship between the initial gas phase connectivity and capillary trapping efficiency. However, the residual gas distribution in the pore structure of porous media at different Ca and S_{wi} remain ambiguous. Also, these micromodels cannot completely characterize the complex pore structure of reservoir rocks.

Recently, NMR relaxometry measurement was introduced to analyze the influences of micropores and initial imbibition rate on S_{gr} [6], and the accuracy of NMR measurement have been fully verified. T_2 relaxation time is related to pore properties, and a corresponding relationship between T_2 relaxation time and pore size can be theoretically derived [27]. The T_2 distribution of a sample saturated by water can be used to characterize its porous structure and evaluate its pore size distribution [28]. Also, the initial water saturation in rock sample can be precisely quantified at the beginning of experiment by NMR measurement [29,30]. Moreover, combining with mercury intrusion (MI) data, the conversion coefficient between T_2 relaxation time and pore size can be further determined [31,32]. Fluid migration in porous media can be monitored at the pore scale in real time by applying NMR. So far, NMR has been successfully applied to analyze the oil recovery ratio under different displacement volumes [33], the residual oil distribution in rock samples [29] and the effect of micro structures on imbibition [32], etc. However, few studies have looked into the microscopic residual gas distribution within rock samples at different S_{wi} and Ca. The interaction between S_{wi} and Ca during imbibition processes is still unknown.

Therefore, spontaneous and forced imbibition experiments are carried out on reservoir sandstone samples with a NMR relaxation system in this work. The NMR transverse relaxation time (T_2)

spectrum was obtained and recorded to monitor the gas saturation changes and their saturation distribution changes during the imbibition processes in samples. The effects of S_{wi} and Ca on residual gas distribution are studied. Combining with mercury intrusion measurements, the NMR T_2 spectrum as a function of pore sizes is determined based on the modified linear relationship of pore size and T_2. Then, the residual gas distribution in pores of rock sample, including micropores ($r < 1$ μm), mesopores (1–10 μm) and macropores ($r > 10$ μm), is quantitatively analyzed. Finally, the trapping mechanisms of gas phase in sandstone samples and the interaction between S_{wi} and Ca during imbibition processes are discussed. Results from this study provide an improved understanding on the processes that affect the development of water-drive gas reservoirs.

2. Imbibition Experiments Theories and Methods

2.1. Material

In this study, two similar samples with similar properties were selected from the same position of a gas reservoir core (defined as samples #1-1 and #1-2). Samples #1-1 and #1-2 were each further cut into two pieces (defined as samples #1-1F and #1-1M, #1-2F and #1-2M). Samples #1-1F and #1-2F are longer, and are used for spontaneous and forced imbibition experiments, while samples #1-1M and #1-2M are shorter and used for mercury intrusion experiments. The size, components, porosity and permeability of each sample are listed in Table 1. The microscopic properties of samples are shown in Figure 1. There appears to be very little difference of the pore structures between samples #1-1F and #1-1M (or samples #1-2F and #1-2M). The range of primary grain diameter is from 80 to 120 μm. Then, the rock samples were salt-washed and dried in an oven at 105 °C until their weights became constant [9,11]. Also, the wettability of rock samples was assumed to be constant before and after waterflooding experiments and drying treatments. Nitrogen gas (99.99%) (termed gas throughout the text) and synthetic brine (termed brine) were selected as the fluid media. The physical properties and composition of the brine are presented in Table 2.

Table 1. Sizes, components and properties of the sandstone samples.

Sample	Mineral Component	Diameter (cm)	Length (cm)	Porosity (%)	Permeability (mD)
#1-1F	55% quartz + 35% feldspar + 10% cement	2.440	4.534	24.01	82.26
#1-1M			2.500		
#1-2F	58% quartz + 34% feldspar + 8% cement	2.451	4.580	22.72	92.22
#1-2M			2.500		

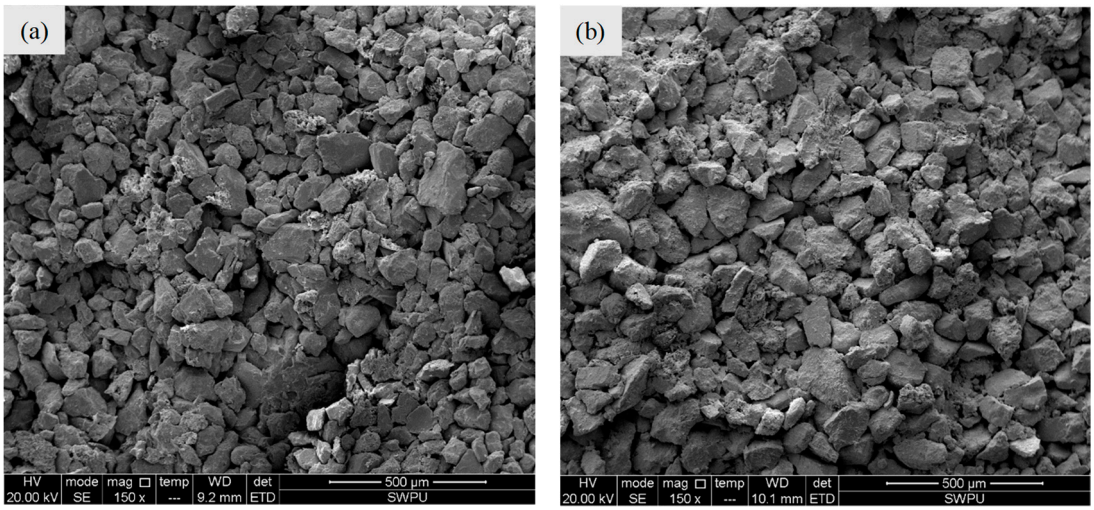

Figure 1. The scanning electron microscopy photos of samples: (**a**) #1-1; (**b**) #1-2.

Table 2. Physical properties and composition of the brine.

Composition	Concentration (mg/L)	Room Temperature and Brine Properties	
Sodium	7863.25	Room temperature (°C)	20.0 ± 1.0
Chlorine	17,717.50	Density (g/mL)	1.03
Potassium	2617.45	Viscosity (mPa·s)	1.0
Calcium	1801.80	Interfacial tension (mN/m)	72.9

2.2. Setup

A high-pressure displacement experimental system (Figure 2) was built to inject fluid into the core samples while real-time NMR images and corresponding data were obtained. The system is primarily composed of the following three parts: (i) a high-pressure fluid delivery system consisting of a ISCO pump (100DX, Teledyne, Thousand Oaks, CA, USA), two storage cylinders (one filling with brine and the other filling with nitrogen) that can reach a certain S_{wi} in samples or inject brine into samples, and a core holder (Niumag, China); (ii) a confining pressuring system including a syringe pump (Series III, Scientific Systems, USA) and a container filled with fluorocarbon oil (supplied by Niumag, China). The syringe pump transports the fluorocarbon oil from the container into the core holder to produce the confining pressure; and (iii) an NMR image and data acquisition system including a computer and an NMR spectrometer (MesoMR23-60H-I, Niumag, China) that can scan and image the entire sample and record the T_2 spectrum at real-time during the processes of waterflooding experiments. The outlet of the core holder is connected to a valve that opens to the ambient atmosphere and the effluent is collected by a graduated cylinder. The basic framework of the NMR device has been described elsewhere by Blümich et al. [34] To avoid interference of the solvent protons in the process of NMR measurement, fluorocarbon oil, composed of only three elements including carbon, fluorine, and oxygen, is used as the confining pressure liquid. In the core holder, polymer heat-shrinkable tube was utilized to seal the samples [29]. The inlet and outlet are covered with copper mesh to avoid magnetic interferences. Moreover, a mercury intrusion apparatus (PoreMaster60, Quantachrome, USA) is used to conduct the mercury intrusion measurements by injecting mercury in a range of pressure from 0 to 413.79 MPa (i.e., 0–60,000 psi).

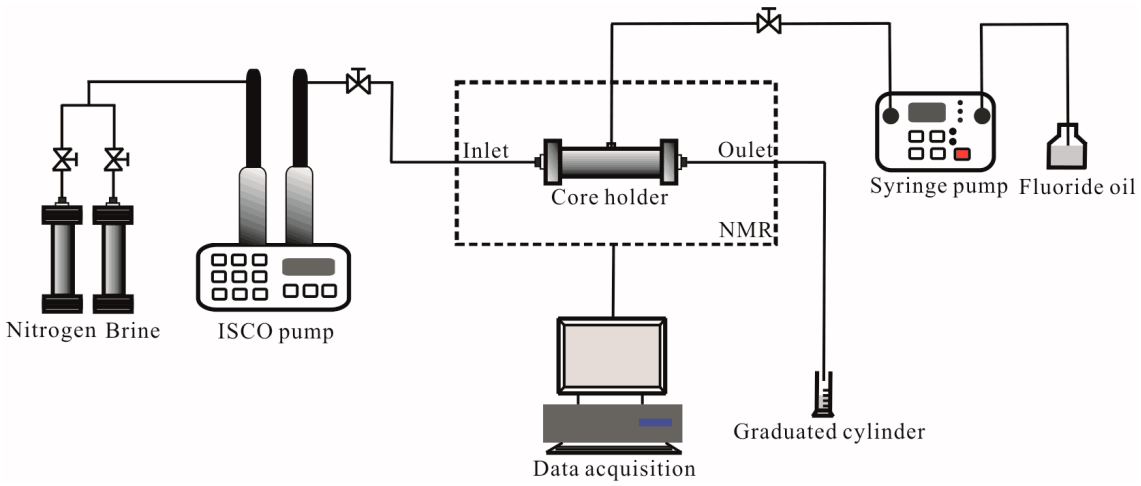

Figure 2. Experimental setup for the forced and spontaneous imbibition experiments.

2.3. Procedures

The experimental procedure of the forced imbibition experiment at $S_{wi} = 0$ is as following: (i) the dried sample, sealed with a heat-shrinkable tube, is placed in the core holder; (ii) the core holder with the sample is placed in the NMR setup. The fluorocarbon oil is injected into the core holder to produce a confining pressure of 2 MPa on the sample; (iii) the brine is injected into the sample at a

specified flowrate (Q = 0.001, 0.01, 0.1, and 1 mL/min, corresponding to 0.28, 2.83, 28.29 and 282.89 pore volumes per day, respectively). The T_2 spectrum is acquired in real-time. The inlet pore pressure and the outlet flow volume are measured simultaneously; (iv) the experiment was stopped when T_2 spectrum showed no further changes. For the forced imbibition experiments at S_{wi} = 39.34 ± 1.57 and 62.98 ± 2.22% (in this work, S_{wi} = 0, 39.34 ± 1.57 and 62.98 ± 2.22% are expressed as S_{wi1}, S_{wi2} and S_{wi3} respectively), the experimental procedures are as following: (i) the dried rock sample was initially immersed into the brine and then vacuumed at 10 MPa over 10 h (i.e., the sample is fully saturated); (ii) then the fully saturated sample was sealed with heat-shrinkable tube and placed in the core holder into the NMR setup with confining pressure of 2 MPa; (iii) the T_2 spectrum of the fully saturated sample was acquired; (iv) then, gas is injected into the sample to displace the brine with continuously increasing flow rates from 0.01 to 1 mL/min and stopped until the desired water saturation (S_{wi2} or S_{wi3}) was reached (the experimental setup was shown in Figure 2); (v) the brine is injected into the sample at a specified flowrate (Q = 0.001, 0.01, 0.1, and 1 mL/min) and the T_2 spectrum is acquired in real-time. The inlet pore pressure and the outlet flow volume are measured simultaneously; (vi) the experiment was stopped as the total amplitudes of the T_2 spectrum are constant. More than two pore volumes of water was injected during imbibition experiments. In each experiment, NMR waiting time is set to 5000 ms, echo time is set to 301 μs, echo number is set to 12,000, scanning number is set to 32 and gain number (the magnification times of signals) is set to 20. After each experiment, the sample was taken out and re-dried in the oven at 105 °C until their weights became constant (over 12 h) [9,11,29]. For the spontaneous imbibition experiment, the experimental procedures are almost the same as the forced imbibition experiment for each corresponding S_{wi}, except for the step of brine injection. The brine was introduced from the upstream end of the sample surface to saturate while T_2 spectrum was continuously recorded until the T_2 spectrum became constant.

A total of 15 imbibition experiments, 12 forced imbibition and three spontaneous imbibition, were carried out at three different S_{wi} (S_{wi1}, S_{wi2} and S_{wi3}) and four magnitudes of Q (0.001, 0.01, 0.1 and 1 mL/min) (Table 3). Samples #1-1F and #1-2F were used for the forced imbibition and the spontaneous imbibition experiments, respectively. All the imbibition experiments were conducted at room temperature (20.0 ± 1.0 °C). The corresponding Darcy's velocity (v), Ca and logCa of the injection rate of brine in the forced imbibition experiments were also shown in Table 3. In addition, samples #1-1M and #1-2M were measured the pore size distribution by mercury intrusion method, respectively.

Table 3. Experimental conditions in spontaneous imbibition and forced imbibition experiments.

S_{wi}(%)	Spontaneous Imbibition	Forced Imbibition				
	Sample	Sample	Q (mL/min)	v (m/d)	Ca	logCa
0 39.34 ± 1.57 62.98 ± 2.22	#1-1F	#1-1F #1-2F	0.001 0.01 0.1 1	0.0129 0.129 1.29 12.9	2.09×10^{-9} 2.09×10^{-8} 2.09×10^{-7} 2.09×10^{-6}	−8.68 −7.68 −6.68 −5.68

2.4. Water/Gas Saturation Measurement Theories and Methods

With the NMR technique, the T_2 spectrum is acquired to illustrate the pore size distribution. The hydrogen protons, one of the two elements of water, can produce nuclear magnetic resonance signals under the adscititious magnetic field, and the signal decay speed is described as relaxation time in NMR physics. The relaxation time denotes the loss of the transverse magnetization with T_2 and the increase of longitudinal magnetization with T_1 [9]. Thus, each sample pore space, occupied by water, can be described by T_2 displayed by the following Equation (1) [32].

$$\frac{1}{T_2} = \frac{1}{T_{2,\text{bulk}}} + \frac{1}{T_{2,\text{surface}}} + \frac{1}{T_{2,\text{diffusion}}} \quad (1)$$

where $T_{2,bulk}$ is the bulk relaxation time (ms), $T_{2,surface}$ is the surface relaxation time (ms) and $T_{2,diffusion}$ is the relaxation time induced by diffusion (ms). In this study, the brine flows through the sandstone sample, $T_{2,bulk}$ and $T_{2,diffusion}$ can be neglected [29]. Then, T_2 is mainly dependent on $T_{2,surface}$, which is associated with the specific surface area of a pore. $T_{2,surface}$ can be expressed as follows [29].

$$\frac{1}{T_{2,surface}} = \rho_2(\frac{S}{V})_{pore} \tag{2}$$

where ρ_2 is the surface relaxivity (μm/ms), S is the pore surface area (μm^2) and V is the pore volume (μm^3). The ratio of S/V can be expressed as the ratio of the dimensionless shape factor for the pore (F_s) and pore radius (μm), as follows [31].

$$\frac{S}{V} = \frac{F_s}{r} \tag{3}$$

Combining Equations (2) and (3), we have

$$T_{2,surface} = \frac{1}{\rho_2 F_s} r \tag{4}$$

For a given sample, its surface relaxivity and shape factor can be assumed to be constant. Thus,

$$T_2 = Cr \tag{5}$$

where $C = 1/(\rho_2 F_s)$. C is a constant conversion coefficient (ms/μm) and can be determined by combining with mercury intrusion method.

In the NMR experiment, the T_2 decay curve, which consists of many exponential decay components can be obtained directly. As for the rock sample composed of various sizes pores that correspond to various decay components, the different pore size is exponential to different T_2. And the sum of magnetization vector is superimposed by magnetization vectors of pore radius [34]:

$$\boldsymbol{M}(t) = \sum_i \boldsymbol{M}_i e^{-t/T_{2i}} \tag{6}$$

where $\boldsymbol{M}(t)$ is the sum of the magnetization vector measured at time t, $\boldsymbol{M}_i$ is the ith magnetization vector corresponding to transverse relaxation time T_{2i}.

Using the inversion technology, the share of different T_2, i.e., the T_2 spectrum of a sample can be calculated based on Equation (6). The abscissa of the T_2 spectrum is the transverse relaxation time (T_2), and the ordinate is the amplitude. and the total amplitude of the T_2 spectrum represents the total pore volume in rock samples. Combining Equations (5) and (6), the amplitude of the T_2 spectrum can be converted into the share of different pores expressed as A_i. The larger the pore size is, the longer the relaxation time T_2 is. Thus, the volumetric percentage of the pores occupied by water in a rock sample after water flooding can be expressed as $A_i/A_{s\,i} \times 100\%$, while the rest volumetric percentage, $(1 - A_i/A_{si}) \times 100\%$, is gas occupying. Where A_{si} is the amplitude of the T_2 spectrum for the sample that is fully saturated by water. Therefore, the S_w in sample during water flooding can be expressed as the percentage of the sum of the T_2 spectrum amplitude from the sum of the T_2 spectrum amplitude for a fully saturated sample. S_{gr} of sample after water flooding is calculated as

$$S_{gr} = 100\% - S_w = 100\% - \frac{\Sigma A_i}{\Sigma A_{si}} \times 100\% \tag{7}$$

Combining Equations (5) and (7), the residual gas distribution in the pore space of a sample can be analyzed. In this study, the pore size distribution curves of samples #1-1M and #1-2M were measured by mercury intrusion method. The maximum pressure of the mercury intrusion was 186 MPa, corresponding to a pore size of 0.004 μm. The conversion coefficient C was obtained by comparing the

weighted average value of the T_2 spectrum of each sample with the corresponding mercury intrusion curve, calculated by the following

$$C = \frac{\sum_i T_{2i}A_i / \sum_i A_i}{\sum_i r_i S_i / \sum_i S_i} \quad (8)$$

where T_{2i} is the NMR transverse relaxation time, A_i is the amplitude of the T_2 spectrum at T_{2i}, r_i is the sample pore radius obtained by mercury intrusion method, and S_i is the mercury injection saturation corresponding to r_i on the mercury intrusion curve, and $\sum_i S_i$ is the maximum mercury injection saturation of sample in mercury intrusion experiment.

3. Results and Discussion

3.1. The T_2 Spectrum

The T_2 spectra of sample #1-1F acquired in spontaneous imbibition experiments at S_{wi1}, S_{wi2} and S_{wi3} are shown in Figure 3a–c, respectively. The measured T_2 spectra represents the properties of the entire rock sample, which reflects water distribution in all of pores in the whole rock sample. In Figure 3a–c, curve I shows the T_2 spectrum of the sample that is fully saturated with brine; curve II shows the T_2 spectrum of the sample at three S_{wi} conditions; and curve III shows the T_2 spectrum of the sample that is completely taken with spontaneous imbibition. To compare curves I and II, most of the initial gas is found existing in the range of 1–100 ms. Comparing curves II and III, it is observed that most of the residual gas is trapped in the range of relaxation time from 10 ms to 100 ms. According to the characteristics of water imbibing into the rock samples during the processes of spontaneous imbibition, the rock samples can be assumed to be strongly water-wet in this work. Subsequently, the S_{gr} in spontaneous imbibition experiments at S_{wi1}, S_{wi2} and S_{wi3} are obtained as 34.02%, 38.84% and 30.89%, respectively. In addition, the relative errors of samples porosity obtained by NMR testing and a routine gas porosity measurement method, which is the base of Boyle's law, are less than 5.33%, which fully validates the accuracy of NMR testing.

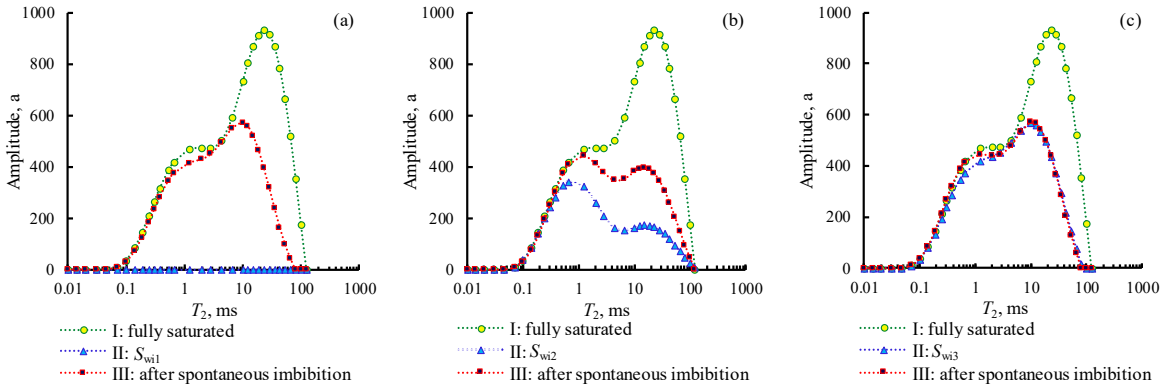

Figure 3. The T_2 spectrum of sample #1-1F that measured in the spontaneous experiments with three S_{wi}: (**a**) S_{wi1} = 0; (**b**) S_{wi2} = 39.34 ± 1.57%; (**c**) S_{wi3} = 62.98 ± 2.22%.

The T_2 spectrums of samples #1-1F and #1-2F acquired in forced imbibition experiments at the same three S_{wi} conditions (0, 39.34 ± 1.57 and 62.98 ± 2.22%) and four waterflooding flow rates (log*Ca* = −8.68, −7.68, −6.68, −5.68) are shown in Figure 4a–c, respectively. In Figure 4, curve I and curve II are the same as those in Figure 3, while curves III, IV, V and VI show that the T_2 spectra of samples #1-1F and #1-2F displaced by the brine with flowrate of log*Ca* = −8.68, −7.68, −6.68 and −5.68, respectively. From Figure 4, the amplitude of the T_2 spectrum increases significantly at log*Ca* = −6.68 and log*Ca* = −5.68, indicating different capillary trapping mechanisms for the sample under different *Ca* conditions. Then, the S_{gr} in forced imbibition experiments at the same three S_{wi} conditions was calculated.

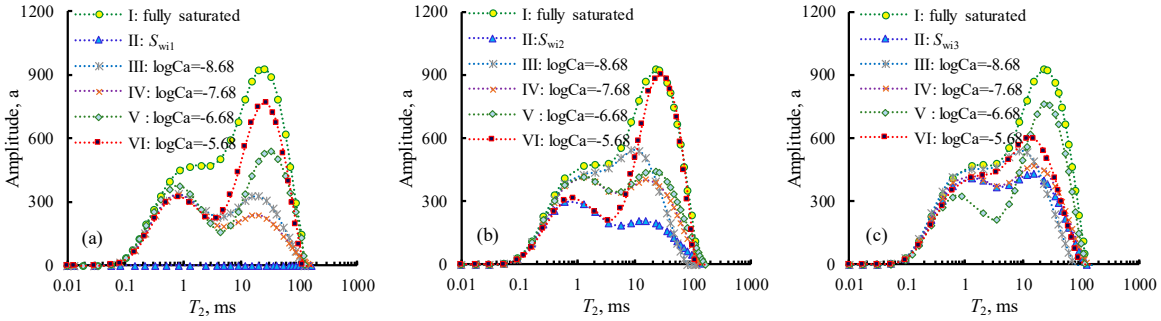

Figure 4. T_2 spectrum of samples #1-1F and #1-2F that measured in the forced imbibition experiments with three S_{wi} and four different flowrates: (**a**) S_{wi1} = 0; (**b**) S_{wi2} = 39.34 ± 1.57%; (**c**) S_{wi3} = 62.98 ± 2.22%. The curve I and curve II in the above pictures only presents the results of sample #1-1F for concise. ((**a**): curves III, IV and VI corresponding to sample #1-2F, curve V corresponding to sample #1-1F; (**b**): curves III, IV, V corresponding to sample #1-1F, curve VI corresponding to sample #1-2F; (**c**) curves III, IV, VI corresponding to sample #1-1F, curve V corresponding to sample #1-2F).

3.2. Pore Radius and Pore Size Distribution

Since each rock sample has its intrinsic conversion coefficient, C, it is impossible to describe the distribution of residual gas in the pore structure of a sample quantitatively by using the T_2 spectrum alone [29]. With the mercury intrusion technique, the pore size distribution of the samples #1-1F and #1-2F, or the samples #1-1M and #1-2M, can be obtained. The pore radius was in the range of 0.004 μm–43 μm with an average of 6.20 μm for sample #1-1F, while the pore radius was between 0.004 μm and 37.17 μm with an average of 6.26 μm for sample #1-2F. Using Equation (8), the conversion coefficients can be calculated. The conversion coefficients of samples #1-1F and #1-2F were 2.87 ms/μm and 3.32 ms/μm, respectively. In this work, the sizes of the sample pores (pore radius) are divided into three scales; < 1 μm, 1–10 μm and > 10 μm, to represent micro-, meso- and macro-pores, respectively [29].

3.3. Initial Water, Produced Gas and Residual Gas Distribution

Based on the induced conversion coefficients and Equations (5) and (8), the pore distribution of initial water, residual gas and produced gas in micro-, meso- and macro-pores in spontaneous imbibition are calculated and plotted in Figure 5, along with their corresponding percentages of pore distribution in each range of pore size. As shown in Figure 5, the sum of initial water, residual gas and produced gas in micro-, meso- and macro-pores represents the total pore space (expressed as 100%). The grey volume represents the percentage of produced gas from the pores of the corresponding size, while the orange is residual gas and the blue is initial water. In spontaneous imbibition experiments: (i) at S_{wi1}, most of gas in micropores (89.62%) and mesopores (70.46%) were produced, while most of the gas in macropores (82.25%) were retained; (ii) at S_{wi2}, most of the micropores (70.49%) were occupied by the initial water that was kept in the micropores all the time, and most of the residual gas remained in meso- and macro-pores; (iii) at S_{wi3}, most of the residual gas were retained in meso- and macro-pores, and most of the initial water were kept in micro- and meso-pores. Namely, gas can be produced from all sizes of pores at S_{wi1} and S_{wi2}. However, no gas was produced from meso- or macro-pores at S_{wi3} (Figure 5). More than 90% of residual gas existed in meso- and macro-pores at all three S_{wi} conditions.

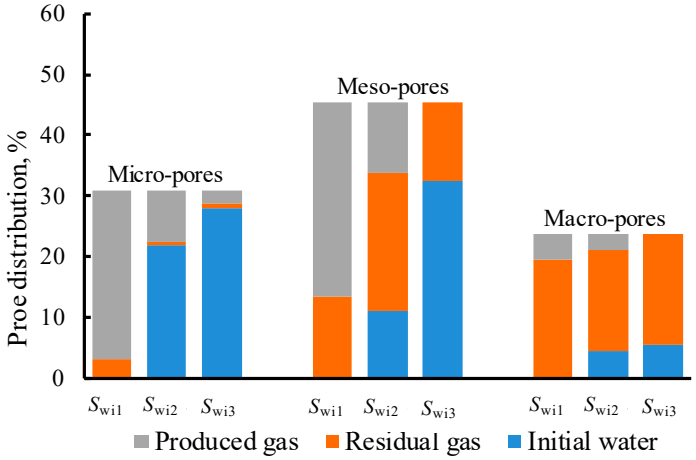

Figure 5. The pore distribution of initial water, residual gas and produced gas in micro-, meso- and macro- pores in spontaneous imbibition experiments of sample #1-1F at different S_{wi}.

In the same way, the pore distribution of the initial gas, residual gas and produced gas in micro-, meso- and macro-pores in forced imbibition at the four log*Ca* and three S_{wi} conditions are also plotted in Figure 6a–c. From Figure 6a, in forced imbibition at S_{wi1} condition, most of the gas in micropores (81.46–87.90%) were produced under all log*Ca* conditions, while most of residual gas was found in meso- (64.91–74.07%) and macro-pores (70.94–74.55%) at low log*Ca* (log*Ca* = −8.68, −7.68). Meanwhile, most of the gas was produced from meso- (68.73%) and macro-pores (76.90%) at high log*Ca* (log*Ca* = −5.68). From Figure 6b, in forced imbibition at S_{wi2} condition, most of the initial water was trapped in micropores (66.44–77.36%), some in mesopores, and a small amount in macropores at any log*Ca*. About half of the gas was trapped in mesopores (44.59–48.26%), and a small amount in micropores. More than half of the macropores (58.00–75.22%) stored the residual gas at low log*Ca* (log*Ca* = −8.68, −7.68) and about half of the gas in macropores could be produced at high log*Ca* (log*Ca* = −5.68). In the case of forced imbibition in the S_{wi3} condition (Figure 6c), most of the initial water was kept in micro- (64.72–92.05%) and meso-pores (55.60–72.75%) at all log*Ca* values, while much of the residual gas were trapped in meso- (25.32–40.73%) and macro-pores (34.66–75.04%) at any log*Ca*. A small amount of gas can be produced from pores in the S_{wi3} condition. Therefore, S_{wi} and *Ca* significantly affect the distributions of residual gas in micro-, meso- and macro-pores, and the amount of gas that can be produced from each size of pores. In addition, we also noticed nonuniform initial conditions for S_{wi3} in forced imbibition experiments. It is very difficult to build identical S_{wi} in the four groups of forced imbibition experiments at the same *Ca*. Therefore, S_{wi} built in rock samples is usually a range for imbibition experiments at the same *Ca*, which can lead to the nonuniform initial conditions. In addition, the hysteresis and capillary end effects can also cause the nonuniform initial conditions [23,35]. However, their influence on the residual gas distribution in rock samples can be negligible compared with *Ca*. The hysteresis and capillary end effects are neglected in this work.

3.4. Impacts of S_{wi} on Residual Gas Distribution

In the spontaneous imbibition experiments, capillary forces dominate the imbibition process [32]. The initial water imbibition rate, defined as the ratio of water imbibition volume and imbibition time from the beginning to the quasi-stable state of spontaneous imbibition experiment, is determined by capillary forces, which are related to the pore structure of the sample and S_{wi} [36]. In this work, the initial water imbibition rate at S_{wi1}, S_{wi2}, and S_{wi3} were obtained as 0.0141 mL/min, 0.0024 mL/min and 0.0008 mL/min, respectively. That is to say, the larger the S_{wi}, the smaller the initial water imbibition rate.

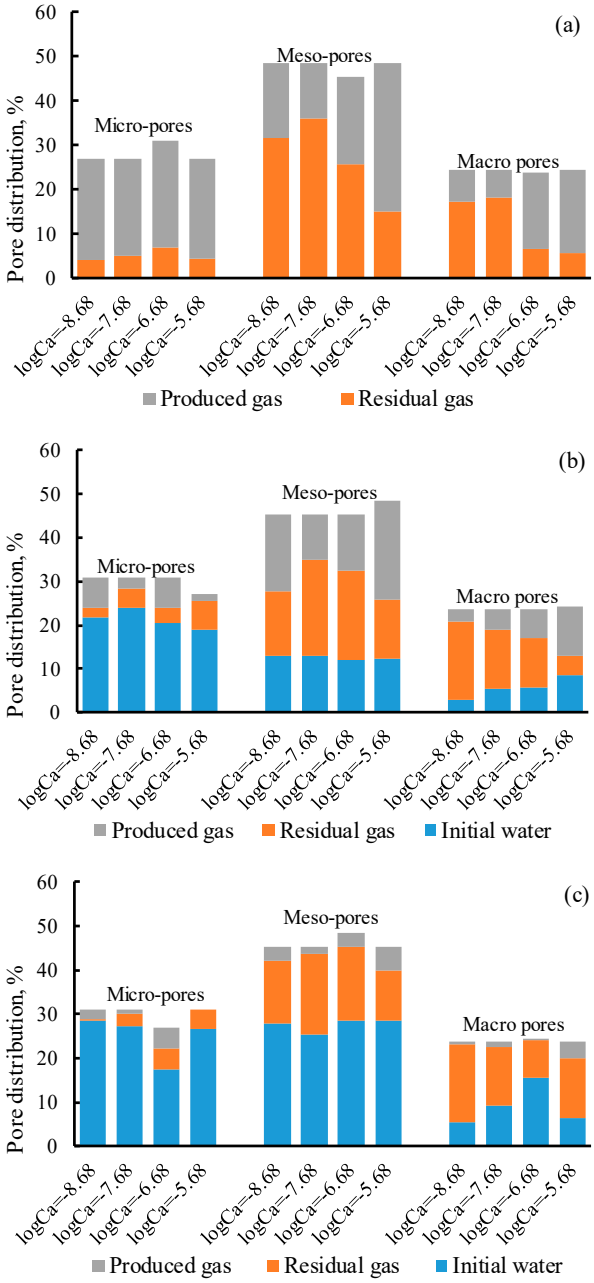

Figure 6. The pore distribution of initial water, residual gas and produced gas in micro-, meso- and macro- pores in forced imbibition experiments of samples #1-1F and #1-2F at different *Ca* and different S_{wi} (the details of experiment samples are consistent with Figure 4): (**a**) $S_{wi1} = 0$; (**b**) $S_{wi2} = 39.34 \pm 1.57\%$; (**c**) $S_{wi3} = 62.98 \pm 2.22\%$.

During the spontaneous imbibition processes, the gas porosity distribution (A_{gi}) in sample at S_{wi1} and S_{wi2}, which is calculated by Equation (9), are shown in Figure 7. In Figure 7, the curves labeled as pore distribution show the porosity distribution of the sample with pore radius, and the sum of porosity distribution represents the total porosity (ϕ) of the sample. The curves labeled with imbibition time (min) represent the gas porosity distribution (A_{gi}) in the sample during spontaneous imbibition experiments, while the curves labeled as residual gas represents the porosity distribution of residual gas. From Figure 7a, a significant decrease of spectral amplitude at the imbibition time of 7 min and 23 min indicated that much of the gas initially found in micro-pores was forced out. Then, the spectral amplitude corresponding to gas in micro- and meso-pores decreased simultaneously at 87 min, 135 min and 167 min. This explains that there is an obvious thin-film flow process ahead of the

bulk flow for the experiment at S_{wi1} (such as 7 min and 23 min). Namely, water first fills the small pores and forms water film on the surfaces of large pores, while the thickness of water film depends on the surface roughness, wettability and interfacial tension [2,36]. Subsequently, the bulk water flow occurs, and bulk flow channels are composed of micro- and meso- pores in samples (87 min, 135 min and 167 min in Figure 7a). Some large gas clusters, initially gathered from thin-film flow, finally fill into the macro-pores surrounded by the bulk water phase. In the end, 90.61% of residual gas remains in the meso- and macro-pores for S_{wi1}, which agrees well with the claim that 85% of residual gas remains as larger gas clusters [18]. Whereas for S_{wi2}, the connectivity of initial gas phase (especially in micro- and meso-pores) is worse. The thin-film flow rarely occurs, as initial water has existed in samples with S_{wi2} (Figure 5), while the bulk water flow slowly occurs during the entire process of the spontaneous imbibition experiment (Figure 7b). The snap-off trapping is more significant with the lower initial water imbibition rate of 0.0024 mL/min [2,24], which leads to more gas (59.19%) trapped in mesopores at S_{wi2}. Although the initial water imbibition rate (0.0008 mL/min) is minimum for S_{wi3}, 90.84% of micropores and 71.47% of mesopores have been occupied by initial water, which indicates that water flow channels have existed in samples from inlet to outlet before the spontaneous imbibition processes (Figure 5). Finally, only 5.42% of the original gas is produced at S_{wi3}, while 97.34% of residual gas exists in meso- and macro-pores (Figure 5). Therefore, residual gas primarily remains in macropores for S_{wi1} (51.52%) and S_{wi3} (54.81%) under spontaneous imbibition, while in mesopores for S_{wi2} (59.19%). However, the residual gas distribution in the pore structure of sample is basically consistent for three S_{wi} in the spontaneous imbibition experiments (Figure 5).

$$A_{gi} = \left(\frac{A_{si} - A_i}{\Sigma A_{si}}\right) \times \phi \tag{9}$$

$$CTE = \frac{S_{gr}}{1 - S_{wi}} \times 100\% \tag{10}$$

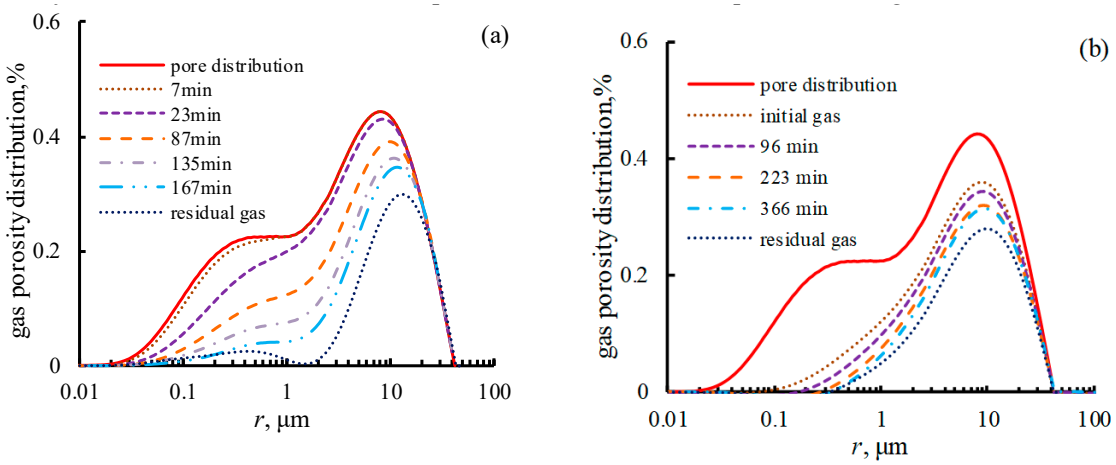

Figure 7. The gas porosity distribution in sample #1-1F during the spontaneous imbibition experiments: (**a**) S_{wi1} = 0; (**b**) S_{wi2} = 39.34 ± 1.57%.

3.5. Impacts of Ca on Residual Gas Distribution

In the forced imbibition experiments, viscous forces increase with the increasing *Ca* [8]. Figure 8 depicts the capillary trapping efficiency (*CTE*) of the gas phase (calculated by Equation (10)) and the experimental time for experiments to reach a stable state in the imbibition experiments. In Figure 8, the green, blue and red solid points represent the spontaneous imbibition experiments (*Ca* is calculated based on the initial water imbibition rate) at S_{wi1}, S_{wi2} and S_{wi3} respectively, while green, blue and red hollow points represent the forced imbibition experiments at S_{wi1}, S_{wi2} and S_{wi3} respectively. *Ca* in spontaneous imbibition experiments is larger when the S_{wi} is smaller. If *Ca* in forced imbibition

experiment is less than that in the spontaneous imbibition experiment at the same condition of S_{wi}, capillary forces will dominate the waterflooding. Otherwise, viscous forces and capillary forces will together control the waterflooding. Figure 8a indicates that the *CTE* increases as S_{wi} increases, and *CTE* at S_{wi3} is 60% higher than that at S_{wi1} in the spontaneous imbibition experiments. Since a small amount of gas (only about 6% of the initial gas) was produced at S_{wi3}, showing a bewildering welter with log*Ca* (Figure 8a), we will focus on S_{wi1} and S_{wi2} conditions in the forced imbibition experiments. Based on the NMR T_2 spectrum (Figure 4), it can also be found that the bulk flow channels are mainly composed of micro- and meso- pores for S_{wi1} and S_{wi2} at log*Ca* = −8.68 and −7.68. At log*Ca* = −6.68, the bulk flow in meso- and macro- pores begins to become obvious. For log*Ca*= −5.68, the T_2 spectral amplitude of meso- and macro-pores most significantly increases, especially for macro-pores. This fact indicates that under the action of viscous forces, the bulk flow channels are mainly composed of meso- and macro- pores for the smaller resistance, and the residual gas in macropores is minimum with log*Ca* = −5.68 for S_{wi1} and S_{wi2} (Figure 6). Meanwhile, comparing Figures 5 and 6, it can be observed that S_{wi} has little influence on the residual gas distribution in spontaneous imbibition experiments, but *Ca* has greater effects (especially in macro- pores) at conditions of S_{wi1} and S_{wi2}. It implies that water flow preferential channels were formed in samples going through the inlet and outlet before imbibition starts to work, *Ca* will not affect the residual gas distribution. The critical *Ca* was not observed from experimental results. In this work, the confining pressure is set as 2 MPa and the pore pressure is less than 0.1 MPa during imbibition experiments. Meanwhile, rock samples used in this work are of high permeability and porosity. Therefore, the influences of rock stress sensitivity and gas slippage effect on the experimental results are negligible. In addition, Figure 8b indicates that the experimental time to reach a stable state increases with increasing S_{wi} in the spontaneous imbibition experiments, which is contrary to the forced imbibition experiments. Meanwhile, the water injection pore volumes (PVs) to reach a stable state are 0.66–1.98, 0.43–1.73 and 0.11–1.08 for S_{wi1}, S_{wi2}, and S_{wi3} in the forced imbibition experiments, respectively, and the PVs increases with increasing *Ca*. The water injection pore volumes to reach a stable state are 0.97, 0.37 and 0.12 for S_{wi1}, S_{wi2}, and S_{wi3} in the spontaneous imbibition experiments, respectively.

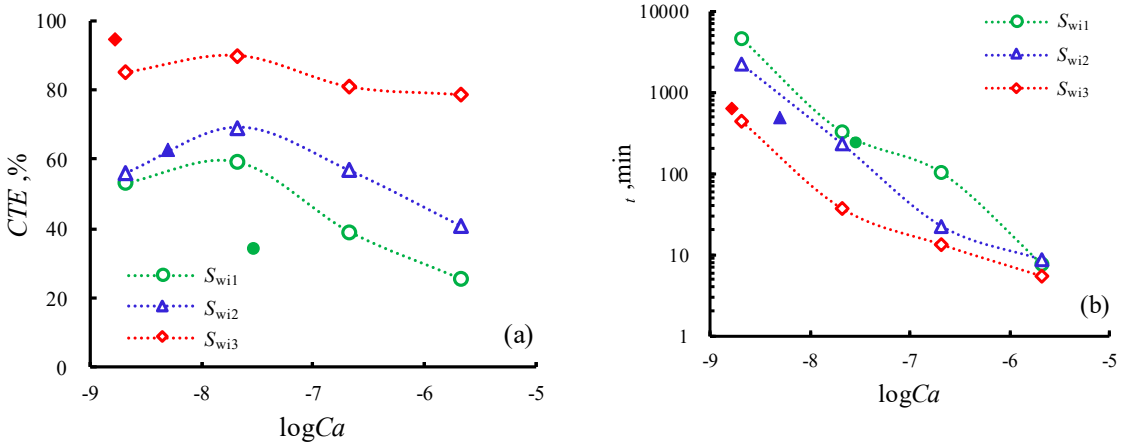

Figure 8. The capillary trapping efficiency and time for experiments to reach a stable state in the imbibition experiments (solid points represent the spontaneous imbibition experiments and hollow points represent the forced imbibition experiments, while the details of experiment samples refer to Figures 3 and 4): (**a**) capillary trapping efficiency; (**b**) the time for experiments to reach stable state.

In conclusion, during spontaneous and forced imbibition processes, most of the residual gas is trapped in larger pores as a continuous or discontinuous phase. *Ca* and S_{wi} jointly determine the residual gas distribution characteristics in rock samples. For a gas reservoir with a lower S_{wi} (such as S_{wi1} and S_{wi2}, which are related to the pore structure and wettability of reservoir rocks), the initial water phase is separately distributed in pores. With reasonable adjustment of gas production rate, the

residual gas in larger pores of reservoir rocks and the *CTE* of reservoir rocks can effectively be reduced so as to raise recovery efficiency of gas reservoirs. However, if S_{wi} in reservoir rocks is at a higher level (such as S_{wi3}), continuous and stable water flow channels will be formed in reservoir rocks, which leads to a high *CTE*. Accordingly, it rarely works to decrease the *CTE* and increase the recovery of gas reservoirs by adjusting gas production rate. The measurement of drainage gas recovery in gas wells should be carried out to improve the recovery of gas reservoirs.

4. Conclusions

In this work, the impacts of *Ca* and S_{wi} on the microscopic residual gas distribution in core samples were investigated by both forced and spontaneous imbibition coupled with NMR. From this study, the following conclusions were drawn.

The conversion coefficients of samples were 2.87 ms/μm and 3.32 ms/μm, respectively. The larger the S_{wi}, the lower the initial imbibition rate. In the spontaneous imbibition experiments, the residual gas distribution is basically consistent for all three S_{wi} (0, 39.34 ± 1.57%, and 62.98 ± 2.22%), and above 90% of residual gas exists in pores larger than 1 μm. In addition, the capillary trapping efficiency of the gas phase increases as S_{wi} increases. The experimental time to reach a stable state increases with increasing S_{wi} in the spontaneous imbibition experiments, which is contrary to the forced imbibition experiments.

Ca significantly impacts the residual gas distribution in the pores of sample. The bulk flow channels are mainly composed of pores smaller than 10 μm at log*Ca* = −8.68 and −7.68. As log*Ca* increases to −5.68, the bulk flow channels are mainly composed of the pores larger than 1 μm. With log*Ca* increasing to −6.68 and −5.68 at S_{wi} = 0 and 39.34 ± 1.57%, the residual gas distribution in pores larger than 10 μm significantly decreases, and that in pores smaller than 1 μm slightly increases. The impact of *Ca* on the residual gas distribution is greater than the S_{wi} for S_{wi} = 0 and 39.34 ± 1.57%, while *Ca* and S_{wi} have little effect on the residual gas distribution for S_{wi} = 62.98 ± 2.22%. This work improves the understanding on the trapping mechanism and water-gas migration in reservoirs.

Author Contributions: Each author has made contributions to the present paper. Conceptualization, methodology and formal analysis, M.L., Y.W. and T.L.; investigation, T.L., J.J. and L.C.; data curation and writing, T.L., Y.W. and Z.W.; supervision and funding acquisition, M.L.

Funding: The project is supported by the open fund (PLN201601) of the State Key Laboratory of Oil and Gas Reservoir Geology and Exploitation (Southwest Petroleum University), the joint fund of the National Natural Science Foundation of China (No. U1562217) and the National Natural Science Foundation of China (No. 41304081).

Conflicts of Interest: The authors declare no conflict of interest.

References

1. Lu, W.Y.; Huang, B.X. Numerical simulation of migration characteristics of the two-phase interface in water-gas displacement. *Energy Explor. Exploit.* **2018**, *36*, 246–264. [CrossRef]
2. Geistlinger, H.; Mohammadian, S.; Schlueter, S. Quantification of capillary trapping of gas clusters using X-ray microtomogrephy. *Water Resour. Res.* **2014**, *50*, 4514–4529. [CrossRef]
3. Meng, Q.B.; Liu, H.Q.; Wang, J. Entrapment of non-wetting phase during co-current spontaneous imbibition. *Energy Fuels* **2015**, *29*, 686–694. [CrossRef]
4. Qian, K.; Yang, S.L.; Dou, H.G.; Wang, Q.; Wang, L.; Huang, Y. Experimental investigation on microscopic residual oil distribution during CO_2 Huff-and-Puff process in tight oil reservoirs. *Energies* **2018**, *11*, 2843. [CrossRef]
5. Wang, L.; Yang, S.L.; Peng, X.; Deng, H.; Meng, Z.; Qian, K.; Wang, Z.L.; Lei, H. An improved visual investigation on gas–water flow characteristics and trapped gas formation mechanism of fracture–cavity carbonate gas reservoir. *J. Nat. Gas Sci. Eng.* **2018**, *49*, 213–226. [CrossRef]
6. Hamon, G.; Suzanne, K.; Billiotte, J.; Trocme, V. Field-wide variations of trapped gas saturation in heterogeneous sandstone reservoirs. In Proceedings of the SPE Annual Technical Conference and Exhibition, New Orleans, LA, USA, 30 September–3 October 2001.

7. Wang, S.; Li, Y.; Sun, L.; Wei, Y.; Wei, X.; Zhang, F. Measurements of residual gas saturation by unidirectional spontaneous imbibitions. *Pet. Sci. Technol.* **2014**, *32*, 2815–2821. [CrossRef]
8. Hekmatzadeh, M.; Dadvar, M.; Emadi, M.A. Visual investigation of residual gas saturation in porous media. *Int. J. Oil Gas Coal Technol.* **2015**, *10*, 161–178. [CrossRef]
9. Ding, M.; Kantzas, A. Capillary number correlations for gas-liquid systems. *J. Can. Pet. Technol.* **2007**, *46*, 27–32. [CrossRef]
10. Lin, H.; Zhang, S.C.; Wang, F.; Pan, Z.Q.; Mou, J.Y.; Zhou, T.; Ren, Z.X. Experimental investigation on imbibition-front progression in shale based on nuclear magnetic resonance. *Energy Fuels* **2016**, *30*, 9097–9105.
11. Suzanne, K.; Hamon, G.; Billiotte, J.; Trocmé, V. Experimental relationships between residual gas saturation and initial gas saturation in heterogeneous sandstone reservoirs. In Proceedings of the SPE Annual Technical Conference and Exhibition, Denver, CO, USA, 5–8 October 2003.
12. Batycky, J.; Irwin, D.; Fish, R. Trapped gas saturations in leduc-age reservoirs. *J. Can. Pet. Technol.* **1998**, *37*, 32–39. [CrossRef]
13. Rezaee, M.; Rostami, B.; Pourafshary, P. Heterogeneity effect on non-wetting phase trapping in strong water drive gas reservoirs. *J. Nat. Gas Sci. Eng.* **2013**, *14*, 185–191. [CrossRef]
14. Kumar, M.; Knackstedt, M.A.; Senden, T.J. Visualizing and quantifying the residual phase distribution in core material. *Petrophysics* **2010**, *51*, 323–332.
15. Suekane, T.; Zhou, N.; Hosokawa, T. Direct observation of trapped gas bubbles by capillarity in sandy porous media. *Transp. Porous Media* **2010**, *82*, 111–122. [CrossRef]
16. Iglauer, S.; Paluszny, A.; Blunt, M.J. Simultaneous oil recovery and residual gas storage: A pore-level analysis using in situ X-ray micro-tomography. *Fuel* **2013**, *103*, 905–914. [CrossRef]
17. Pentland, C.H.; Itsekiri, E.; Al Mansoori, S.K.; Iglauer, S.; Branko, B.; Blunt, M.J. Measurement of nonwetting-phase trapping in sandpacks. *SPE J.* **2010**, *15*, 274–281. [CrossRef]
18. Geistlinger, H.; Mohammadian, S. Capillary trapping mechanism in strongly water wet systems: Comparison between experiment and percolation theory. *Adv. Water Resour.* **2015**, *79*, 35–50. [CrossRef]
19. Tiab, D.; Donaldson, E.C. *Petrophysics*, 2nd ed.; Gulf Professional Publishing: Houston, TX, USA, 2004; p. 352.
20. Guo, H.; Dou, M.; Wang, H.Q.; Wang, F.Y.; Gu, Y.Y.; Yu, Z.Y.; Wang, Y.S.; Li, Y.Q. Proper Use of Capillary Number in Chemical Flooding. *J. Chem.* **2017**, *4307368*, 1–11. [CrossRef]
21. Zendehboudi, S.; Chatzis, I. Experimental Study of Controlled Gravity Drainage in Fractured Porous Media. *J. Can. Pet. Technol.* **2011**, *50*. [CrossRef]
22. Shen, Y.H.; Ge, H.K.; Meng, M.M.; Jiang, Z.X.; Yang, X.Y. Effect of water imbibition on shale permeability and its influence on gas production. *Energy Fuels* **2017**, *31*, 4873–4980. [CrossRef]
23. Mohammadian, S.; Geistlinger, H.; Vogel, H.J. Quantification of Gas-Phase Trapping within the Capillary Fringe Using Computed Microtomography. *Vadose Zone J.* **2015**, *14*. [CrossRef]
24. Buchgraber, M.; Kovscek, A.R.; Castanier, L.M. A study of microscale gas trapping using etched silicon micromodels. *Transp. Porous Med.* **2012**, *95*, 647–668. [CrossRef]
25. Geistlinger, H.; Ataei-Dadavi, I.; Vogel, H.J. Impact of surface roughness on capillary trapping using 2D-micromodel visualization experiments. *Transp. Porous Med.* **2016**, *112*, 207–227. [CrossRef]
26. Herring, A.L.; Andersson, L.; Schlüter, S.; Sheppard, A.; Wildenschild, D. Efficiently engineering pore-scale processes: The role of force dominance and topology during nonwetting phase trapping in porous media. *Adv. Water Resour.* **2015**, *79*, 91–102. [CrossRef]
27. Yuan, Y.; Rezaee, R.; Verrall, M.; Hu, S.Y.; Zou, J.; Testmanti, N. Pore characterization and clay bound water assessment in shale with a combination of NMR and low-pressure nitrogen gas adsorption. *Int. J. Coal Geol.* **2018**, *194*, 11–21. [CrossRef]
28. Slijkerman, W.F.J.; Hofman, J.P. Determination of surface relaxivity from NMR diffusion measurements. *Magn. Reson. Imaging* **1998**, *16*, 541–544. [CrossRef]
29. Yang, P.; Guo, H.K.; Yang, D.Y. Determination of residual oil distribution during waterflooding in tight oil formations with NMR relaxometry measurements. *Energy Fuels* **2013**, *27*, 5750–5756. [CrossRef]
30. Testamanti, M.N.; Rezaee, R. Determination of NMR T2 cut-off for clay bound water in shales: A case study of Carynginia Formation, Perth Basin, Western Australia. *J. Pet. Sci. Eng.* **2017**, *149*, 497–503. [CrossRef]
31. Xu, H.J.; Fan, Y.R.; Hu, F.L.; Li, C.X.; Yu, J.; Liu, Z.C.; Wang, F.Y. Characterization of pore throat size distribution in tight sandstones with nuclear magnetic resonance and high-pressure mercury intrusion. *Energies* **2019**, *12*, 1528. [CrossRef]

32. Lyu, C.H.; Wang, Q.; Ning, Z.F.; Chen, M.Q.; Li, M.Q.; Chen, Z.L.; Xia, Y.X. Investigation on the application of NMR to spontaneous imbibition recovery of tight sandstones: An experimental study. *Energies* **2018**, *11*, 2359. [CrossRef]
33. Chen, T.; Yang, Z.M.; Luo, Y.T.; Lin, W.; Xu, J.X.; Ding, Y.H.; Niu, J.L. Evaluation of displacement effects of different injection media in tight oil sandstone by online nuclear magnetic resonance. *Energies* **2018**, *11*, 2836. [CrossRef]
34. Blümich, B.; Casanova, F.; Appelt, S. NMR at low magnetic fields. *Chem. Phys. Lett.* **2009**, *477*, 231–240. [CrossRef]
35. Andersen, P.Ø.; Standnes, D.C.; Skjæveland, S.M. Waterflooding oil-saturated core samples-Analytical solutions for steady-state capillary end effects and correction of residual saturation. *J. Pet. Sci. Eng.* **2017**, *157*, 364–379. [CrossRef]
36. Kibbey, T.C.G. The configuration of water on rough natural surfaces: Implications for understanding air-water interfacial area, film thickness, and imaging resolution. *Water Resour. Res.* **2013**, *49*, 4765–4774. [CrossRef]